Acta Geotechnica
https://doi.org/10.1007/s11440-026-03127-x

RESEARCH PAPER

A hydro-mechanical model for compound slow-moving rockslides with pre-existing open fractures

Alessio Ferrari[1,2] · **Marco Rosone**[1] · **Giorgio Manno**[1] · **Maurizio Ziccarelli**[1] · **Francesco Ronchetti**[3] · **Alessandro Corsini**[3]

Received: 16 January 2026 / Accepted: 8 May 2026

Abstract

This paper presents a model for a unified hydro-mechanical analysis of the behaviour of compound slow-moving rockslides in the pre-failure and post-failure phases. The rockslide is described through several interacting blocks, separated by pre-existing open fractures, which move on an inclined surface. Each block is assumed to be rigid, and the fracture network is composed of vertical fractures which communicate through the basal fractures. Several key features are incorporated in the model, such as the storage of water within the fractures, viscosity and shear strength along the sliding surfaces, as well as the temporal diffusion of water pressure at the base of the landslide bodies. Moreover, the water-squeezing effect, due to the balance of the volume of water when the fractures change their apertures, is accounted for. Following the presentation of the model and its analytical formulation, a sensitivity analysis is conducted to assess how variations in different parameters influence the model's outcomes. The results of 125 simulations across 9 different scenarios, including single- and multi-block systems, were analysed and discussed. Furthermore, the model has been applied to analyse the displacement patterns associated with rainfall for a complex rockslide that occurred in the Northern Apennines in Italy, for which the model parameters were calibrated through a back analysis procedure applied to the monitoring data. The analysis of the obtained results proves that realistic simulations of slow-moving rockslide displacements can be obtained with the presented model.

Keywords Block sliding · Hydro-mechanical modelling · Pre-existing fractures · Rockslides · Water pressure in fractures

List of symbols

α	Slope angle (°)
b	Dimensionless parameter for the solution of diffusion equation (–)
d_{i}	Infiltration duration (day)
D	Diffusion coefficient (m^2/year)
Δt	Time step (day)
F_i	Safety factor for the block ith (–)
F_{vi}	Viscous force for the block ith (kN)
$f(t)$	Fracture aperture as a function of the time (m)
$f_{\min}$	Minimum aperture of the fracture (m)

✉ Alessio Ferrari
alessio.ferrari@unipa.it

Marco Rosone
marco.rosone@unipa.it

Giorgio Manno
giorgio.manno@unipa.it

Maurizio Ziccarelli
maurizio.ziccarelli@unipa.it

Francesco Ronchetti
francesco.ronchetti@unimore.it

Alessandro Corsini
alessandro.corsini@unimore.it

[1] Department of Engineering, University of Palermo, Viale delle Scienze, Ed. 8, 90128 Palermo, Italy

[2] Ecole Polytechnique Fédérale de Lausanne, EPFL, ENAC IIC LMS, GC D1 402 (Bâtiment GC) Station 18, 1015 Lausanne, Switzerland

[3] Department of Chemical and Geological Sciences, University of Modena and Reggio Emilia, via Campi 103, 41125 Modena, Italy

f_i^0	Initial fracture aperture *i*th (m)
φ'	Interface shear strength angle (°)
φ_r'	Interface shear strength angle at residual condition (°)
g	Gravity acceleration (m/s^2)
γ	Unit weight of rock (kN/m^3)
γ_w	Specific weight of the water (kN/m^3)
H_i	Height of the block *i*th (m)
$h_i(t)$	Water column height *i*th as a function of the time (m)
h_i^0	Initial water level in the fracture *i*th (m)
η	Dynamic viscosity (kPa s/m)
q	Infiltration intensity (mm/day)
$k(f)$	Permeability of the fracture (m/day)
k_{min}	Minimum permeability of the fracture (m/day)
λ	Model parameter for the fracture permeability (m/day)
L_i	Width of the block *i*th (m)
M_i	Mass of the block *i*th (t)
N'_i	Normal effective force on the block *i*th (kN)
n	Model parameter for the fracture permeability (–)
S_{ui}	Resultant of the water pressure distribution along the head side of the block *i*th (kN)
S_{di}	Resultant of the water pressure distribution along the toe side of the block *i*th (kN)
S_i	Displacement of the block *i*th (mm)
s_{i-1}	Displacement of the block $i-1$th (mm)
T_i	Mobilised shear force at the base of the block *i*th (–)
T_{fi}	Available shear force (at failure) of the block *i*th (–)
t	Time (day)
U_{bi}	Resultant force of the water pressure distribution at the base of the block *i*th (kN)
u_e	Excess of the water pressure at the time t (kPa)
u_0	Excess of the water pressure at the time $t = 0$ (kPa)
$\overline{u}_t$	Average degree of diffusion (kPa)
u_w	Water pressure (kPa)
u_j	Local degree of diffusion (–)
v_i	Block velocity of the block *i*th (m/s)
V_i	Water volume in the fracture *i*th (m^3)
W_i	Weight of the block *i*th (kN)
y_i	Coordinate of a point located at the base of the block (m)
z	Thickness of the shear band (m)

1 Introduction

The instability of fractured rock slopes represents a significant hazard in many regions worldwide, threatening infrastructure and communities' safety, especially when large volumes of material and complex landslide mechanisms are involved. To add further complexity to the analysis and modelling of this type of instability, landslide bodies can often move slowly or remain dormant over time, though they can suddenly accelerate under certain conditions, such as heavy rainfall or seismic events. Recent studies have explored the mechanics of rockslides through advanced modelling approaches. Spreafico et al. [26] conducted a back analysis of the 2014 San Leo landslide, combining terrestrial laser scanning surveys with 3D distinct element modelling to reconstruct collapse processes. Carlà et al. [4] analysed the mechanisms of block instability at the toe of slowly deforming rock slopes, highlighting the interactions between progressive deformation and block kinematics. Additionally, a study by Deng et al. [9] examined the efficiency of thermochemical pressurization in a rockslide, emphasising the role of thermo-mechanical processes in landslide triggering. Song et al. [25] proposed an extended Newmark sliding block model to evaluate seismic displacements in bedding rock slopes, while Zhou and Zhao [33] explored the progressive failure mechanisms and stability of rockslides through a 3D finite difference numerical simulation.

Among the types of instability in fractured rock masses, compound rockslides present specific peculiarities. They are characterised by multiple volumes of rock, separated by pre-existing open fractures, sliding on a failure surface. The sliding surface is usually planar and is located at the base of the rock blocks or it can develop along weaker inter-stratum within the formation [13]. The deformations within the sliding masses are in general null or negligible, so that the masses can be considered as rigid blocks. Due to their discontinuous nature, the application of modelling approaches based on Continuum Mechanics [15, 21, 24, 29] is often unfavourable for this type of landslide, making it suitable to simulate the landslide as a system of interacting blocks. For example, Picarelli et al. [20], Corominas et al., [5], Alonso and Gens [2], Ferrari et al. [11], Rosone et al. [22] and Troncone et al. [30] have modelled translational slides in which the landslide body, although consisting of soil, is modelled as a series of blocks, sliding along different portions of the slip surface. These models use the evolution of pore water pressures along the sliding surface as input data and, by incorporating the effect of viscous forces on the landslide surface, compute the displacement's evolution in the post-failure stage.

In this paper, a model for slow-moving compound rockslides is presented, in which the landslide body is assumed to be composed of rigid blocks sliding on an inclined plane. We refer here to slow-moving compound rockslides following the definitions provided by Hungr et al. [13]. In order to account for the fundamental role of the water levels in the discontinuities [14, 32], unlike previous applications of the interacting-block approach, we conceived and implemented a new model which incorporates the presence of the pre-existing open fractures (joints) that separate the rock blocks, allowing water infiltration. The considered fracture network is composed by vertical fractures which communicate through the basal fractures. Lateral water flow from the sides of the vertical fractures is included to account for out-of-plane flow, thereby overcoming the limitations of representing realistic flow conditions within a two-dimensional geometry. Water velocities within the vertical fractures are assumed small so that linear distributions of water pressure are assumed. Changes in the distances between the blocks contribute to variations in the water level in the vertical fractures and, consequently, to the resulting forces from water pressure distributions on the boundaries of the blocks. The model also incorporates the nonlinear time-delayed diffusion of the water pressure at the contact between the base of the block and the underlying formation. These features make the model a hydro-mechanical coupled one, as it incorporates the coupling among the diffusion of water pressure along the block bases, the kinematic behaviour of the sliding blocks, and the change in the aperture of the vertical fractures. To the authors' knowledge, this combination of processes has not been explicitly accounted for in existing interacting–block models for slow-moving landslides, representing a novel aspect of the proposed framework. After the model is introduced, its distinctive features are presented, and a sensitivity analysis is performed to highlight the influence of the various parameters on the simulated landslide activity. The application of the model to a back analysis, referencing a real compound rockslide [6], is then discussed to evaluate its ability to capture the observed behaviour after parameters calibration.

2 Model formulation

2.1 Geometry and mechanics of the model

The model is intended to analyse translational landslides featuring fractured rock masses, specifically addressing scenarios where multiple rigid blocks can slide along a common basal discontinuity. The model geometry is given in Fig. 1a where three rigid blocks slide on a plane inclined by α, and they are separated by vertical fractures. Each block has the shape of a parallelogram with a vertical height equal to H_i and a base length equal to L_i. The number and the geometry of the blocks, as well as the inclination of the fractures, can be adjusted as needed, with a simple reworking of the equations presented in the following. Each fracture has an aperture equal to f_i and is filled with water up to the average height h_i, measured from the bottom of the fracture.

The model is 2D. Figure 1b depicts the system of forces acting on the block i, i.e. the weight of the block ($W_i = \gamma H_i L_i \cos\alpha$, being γ the unit weight of the block material), the resultant forces of the water pressures along the upward (S_{ui}) and downward fractures of the block (S_{di}), the resultant forces of the water pressures (U_{bi}), the normal effective stresses (N_i') and the shear stress (T_i) at the base of the block, and the viscous force (F_{vi}) acting along the base when the block moves. When the blocks are not in contact with each other, they interact only through the forces S_{ui} and S_{di}. The velocities of the blocks are represented by the vectors with magnitude v_i depicted in Fig. 1a, b.

In the following sections, the approaches used for analysing the motion of each block and computing the resultant forces from pore water pressures in the fractures are illustrated in detail. The computation of the nonlinear and time-dependent water pressure distribution at the base of the block, obtained through a diffusion model, is reported in Appendix A.

2.2 Stability and motion of the blocks

The stability of each block is assessed by computing its safety factor F_i with a classical limit equilibrium analysis. The equilibrium in the directions perpendicular and parallel to the slope provide

$$N_i' = W_i \cos\alpha - U_{bi} - (S_{ui} - S_{di}) \sin\alpha \tag{1}$$

$$T_i = W_i \sin\alpha + (S_{ui} - S_{di}) \cos\alpha \tag{2}$$

A cohesionless failure criterion is used to quantify the maximum shearing resistance, so that $T_{fi} = N_i' \tan\varphi'$, where the shear strength angle at the interface φ' is assumed to be identical for all the blocks. The safety factor of the block (F_i) is computed as the ratio:

$$F_i = T_{fi}/T_i = [W_i \cos\alpha - U_{bi} - (S_{ui} - S_{di}) \sin\alpha] \tan\varphi' / [W_i \sin\alpha + (S_{ui} - S_{di}) \cos\alpha] \tag{3}$$

An explicit finite difference scheme and a mass balance of the water in the fractures is used for computing both the motion of the block and the variation of resultant force

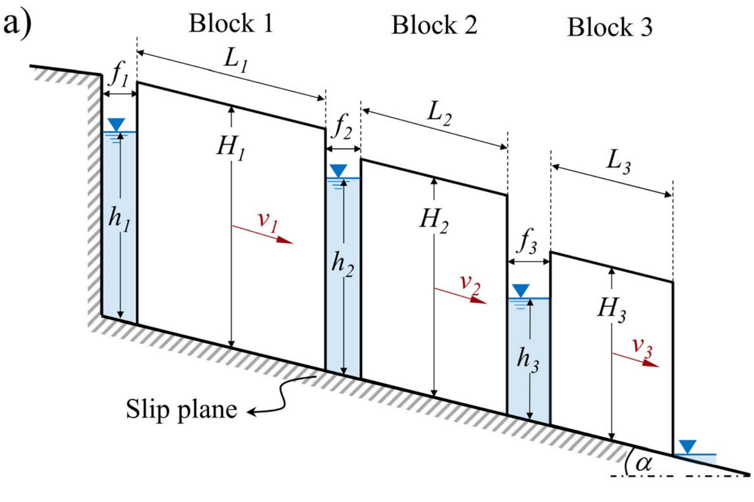

Fig. 1 Schematisation of the landslide body consisting of three blocks sliding on a slip plane (**a**) and of the system of forces acting on the generic block i (**b**)

from the water pressure distributions S_{ui}, S_{di} and U_{bi}. For each time increment Δt, the stability of each block is assessed computing its safety factor; if the computed safety factor is less than one, the block moves and the available shear strength at the base is entirely mobilised. In this regard it is worth specifying that, for the considered block velocities, any excess of pore water pressure at the base potentially induced by the block movements is not taken into account.

The equation of balance of the linear momentum writes

$$\begin{aligned} & W_i \sin\alpha + (S_{ui} - S_{di})\cos\alpha \\ & \quad - [W_i \cos\alpha - U_{bi} - (S_{ui} - S_{di})\sin\alpha]\tan\varphi' - F_{vi} \\ & \quad = M_i \Delta v_i / \Delta t \end{aligned} \tag{4}$$

where M_i is the mass of the block ($M_i = W_i/g$, g is the gravity acceleration). This equation is not subject to a Courant–Friedrichs–Lewy (CFL) type condition [10, 18]. The only numerical constraint on the time step Δt arises from the numerical solution of the diffusion equation used to compute the resultant of the water pressure distribution at the base of the block U_{bi}, as detailed in Appendix A. The selected time step also depends on the resolution of the time-dependent input (see Sect. 2.3). The viscous force can be computed in accordance with the rheological properties of the material at the shear zone; in the following a Bingham's behaviour is assumed, so that the viscous force is

$$F_{vi} = (\eta/z) L_i v_i \tag{5}$$

where η is the dynamic viscosity and z is the thickness of the shear zone. The viscosity terms introduce a rate-dependent contribution, which is considered only when the block is in incipient motion and is strictly dependent on its velocity. This contribution is crucial for simulating slow-moving, deep-seated, or clayey landslides, where deformations are slow and develop over time. In fact, viscosity helps to model phenomena such as continuous sliding even under constant stresses (creep) and gradual acceleration of movement in response to changes in pore water pressure or intense infiltration periods.

Equation (4) is used to compute the block velocity considering all forces constant within the time step:

$$v_i^t = \{W_i \sin\alpha + (S_{ui} - S_{di})\cos\alpha - [W_i \cos\alpha - U_{bi} - (S_{ui} - S_{di})\sin\alpha]\tan\varphi'\}\Delta t + M v_i^{t-\Delta t} / [M_i + (\eta/z) L_i \Delta t] \tag{6}$$

The accumulated displacement of each block (s_i) is then computed, and the aperture of the fractures updated:

$$f_i = f_i^0 + s_i - s_{i-1} \tag{7}$$

where f_i^0 is the initial aperture of the fracture. The resultants of water pressures are then updated as described in the next section. When the safety factor of a block reaches or exceeds one, and the computed velocity is below a specified tolerance, the velocity is set to zero. Although the model refers to a simple scheme with a uniform basal surface slope, it can be easily adapted to a more complex geometry, where each block has a different basal angle and, consequently, slides along a different inclined plane. This can be implemented because the equilibrium and motion of each block are considered separately.

2.3 Calculation of the resultant forces from water pressures

A mass balance of the water in the fractures is used to compute the evolution of the water pressures and thus their resulting forces. The blocks are assumed to be impermeable in the sense that, in this version of the model, flow through the blocks is not possible. As shown in Fig. 2a, the model incorporates a water inflow $q(t)$ into and a water outflow from the fracture. The outflow accounts for lateral water flow from the sides of the fracture, addressing the limitation of representing true flow conditions in a two-dimensional geometry.

In this version of the model, the flow of water through the shear zone is not considered in the water mass balance, as this flow is expected to be minimal; however, this feature can be easily implemented if needed. The outflow is assumed to depend on the height of the water column $h_i(t)$ and on a coefficient $k(f)$, which can be considered as a permeability for the lateral flow from the fracture. The latter is dependent on the aperture of the fracture as depicted in Fig. 2b:

$$k = k_{\min}\{1 + \lambda[(f_i - f_{\min})/f_{\min}]^n\} \tag{8}$$

where k_{min} is the permeability related to the minimum aperture of the fracture f_{min} (here assumed equal to 0.01 m), λ and n are the model parameters. For a unitary thickness, at a given time t, the water volume in the fracture i is computed as

$$V_i(t) = h_i(t) f_i(t) \tag{9}$$

At the time $t + \Delta t$, it becomes

$$\begin{aligned} V_i(t+\Delta t) &= [h_i(t) + \Delta h_i]\,[f_i(t) + \Delta f_i] \\ &= h_i(t) f_i(t) + q(t) f_i(t)\Delta t - k f_i(t)\, h_i(t)\,\Delta t \end{aligned} \tag{10}$$

where $q(t) f_i\,\Delta t$ and $k_i f_i(t)\,h_i(t)\Delta t$ represent the infiltrated and outflown water volume in Δt, respectively. From.

Equation (10), neglecting the term $\Delta h_i\,\Delta f_i / f_i$, the variation of water level in the fracture Δh_i can be computed as:

$$\Delta h_i = q(t)\Delta t - k_i h_i \Delta t - h_i(t)\Delta f_i / f_i(t) \tag{11}$$

The last term $-h_i(t)\Delta f_i / f_i$ represents a "squeezing effect" that accounts for the influence of the change in the fracture aperture on the water column level; this effect results from the possibility of the blocks to move at different velocities, thereby accumulating different displacements (see Eq. 7). If the computed h_i exceeds the block height, it is set equal to that height.

For each fracture, the resultant forces of the water pressures are computed assuming a linear distribution of the pressure of water (u_w) with the depth along h_i; according to the scheme reported in Fig. 1b, the same resultant force from the water pressure distribution within a fracture is applied to both the upstream and downstream blocks (i.e. $S_{ui} = S_{di-1}$). The pressures at the bottom of the fractures are used to compute the water pressure distribution along the base; to account for the possible presence of different materials within the basal zone, such as a saturated soil from the underlying formation, the diffusion of the pressure variations applied at the edges of the base (points P and Q in Fig. 2a) is analysed with a simplified one-dimensional model that incorporates the diffusion coefficient D of the material in the shear zone. The time-dependent diffusion model is detailed in Appendix A. From the nonlinear computed pressure distribution at the base of

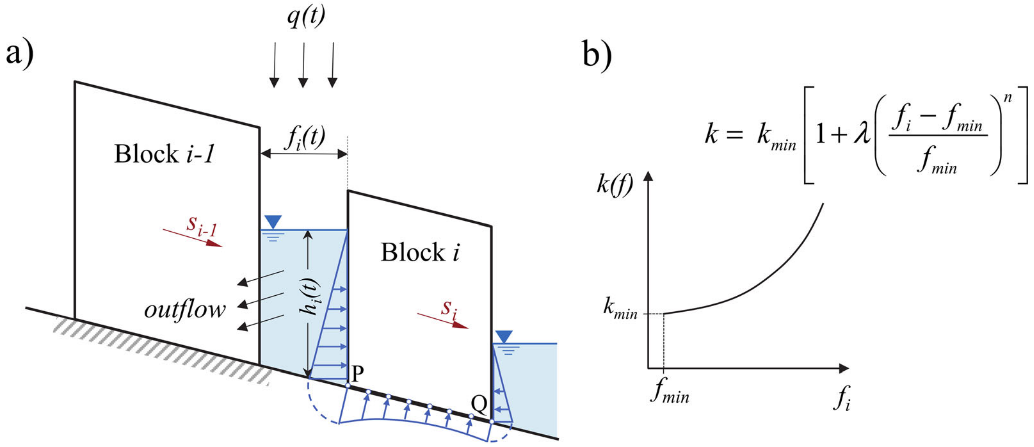

Fig. 2 Schematisation of the water mass balance strategy adopted to compute the water pressure regime in the vertical fractures and at the base of blocks (**a**). Permeability function of the vertical fractures (**b**)

Table 1 Parameters used in the single block simulations

Parameter	Single block					
	Case 1	Case 2a	Case 2b	Case 2c	Case 3a	Case 3b
q (mm/day)	20	60	60	30	40	40
d_i (day)	30	10	10	60	30	30
L (m)	3	3	3	3	1, 2, 3, 4, 5	Var
H (m)	2	2	2	2	var	1, 2, 3, 4, 5
L/H (–)	1.5	1.5	1.5	1.5	$0.2 - 7$	$0.2 - 7$
γ (kN/m^3)	25	25	25	25	25	25
α (°)	11	11	11	11	19	19
φ' (°)	14	14	14	$19 \rightarrow 11$ $19 \rightarrow 15$ $19 \rightarrow 19$	20	20
f_1^0(m)	0.1	0.1	0.1	0.1	0.1	0.1
h_1^0(m)	0.8	0.8	0.8	0.8	0.15	0.15
$k_{\min}$(m/day)	$1{\cdot}10^{-4} - 1{\cdot}10^{-3}$	$1{\cdot}10^{-4}$	$1{\cdot}10^{-4}$	$1{\cdot}10^{-4}$	$1{\cdot}10^{-4}$	$1{\cdot}10^{-4}$
λ (−)	1	1	1	1	1	1
n (−)	1	1	1	1	1	1
η/z (kPa s m^{-1})	$1{\cdot}10^7$	$1{\cdot}10^6 - 1{\cdot}10^7$	$1{\cdot}10^7$	$1{\cdot}10^7$	$1{\cdot}10^7$	$1{\cdot}10^7$
D (m^2/year)	20	20	2; 40; immediate diffusion	10	2	2
Δt (day)	0.2	0.2	0.2	0.2	0.2	0.2
v_i (m/s)	0	0	0	0	0	0

the block, U_{bi} is computed at each time step. An example of an algorithm for implementing the model in the case of a single block case is provided in Appendix B.

3 Model performance

The performance of the model is evaluated and discussed in this section. Initially, a sensitivity analysis is performed. First, a set of idealised cases is presented with reference to a single block to highlight the effects of various modelling features and to evaluate the influence of the parameter variations, such as the fracture lateral permeability, the basal hydro-mechanical parameters (shear strength angle, diffusion coefficient and viscosity) and the block geometry. Next, cases with multiple blocks are examined to analyse some behaviours of compound rockslides. Previous research has shown that determining the viscosity parameter experimentally at the laboratory scale is ineffective, particularly in the case of slow-moving landslides, suggesting that its calibration should be performed at the real scale through a back-analysis of the monitored displacements [11, 31]. Then, the model is applied to a real case study known as the Piagneto compound rockslide [6], with the aim of providing a set of calibrated model parameters specific to the case study and proving the applicability of the modelling approach in capturing the observed

Table 2 Parameters used in the compound rockslide simulations

	Single block	Double block	Triple block
Parameter	Case 4a	Case 4b	Case 4c
q (mm/day)	60	60	60
d_i (day)	10	10	10
$L_1 \times H_1$ (m x m)	10×5	10×5	10×5
$L_2 \times H_2$ (m x m)	–	6×4	6×4
$L_3 \times H_3$ (m x m)	–	–	15×3
γ (kN/m^3)	25	25	25
α (°)	19	19	19
φ' (°)	20	20	20
$f_1^0;f_2^0;f_3^0$(m)	0.1	0.1	0.1
h_1^0(m)	0.7	0.7	0.7
h_2^0(m)	–	0.4	0.4
h_3^0(m)	–	–	0.3
$k_{\min}$(m/day)	$1{\cdot}10^{-4}$	$1{\cdot}10^{-4}$	$1{\cdot}10^{-4}$
λ (−)	1	1	1
n (−)	1	1	1
η/z (kPa s m^{-1})	$1{\cdot}10^7$	$1{\cdot}10^7$	$1{\cdot}10^7$
D (m^2/year)	40	40	40
Δt (day)	0.2	0.2	0.2
v_i (m/s)	0	0	0

Table 3 Parameters used in the Piagneto compound rockslide simulations

Piagneto compound rockslide			
Parameter	Value	Assessed	Calibrated
q (mm/day)	Measured rainfall	✔	
d_i (day)	920	✔	
$L_1 \times H_1$ (m × m)	58.9 × 67.3	✔	
$L_2 \times H_2$ (m × m)	43.8 × 39.4	✔	
$L_3 \times H_3$ (m × m)	41.1 × 26.7	✔	
γ_i (kN/m^3)	25	✔	
α (°)	13	✔	
Δt (day)	1	✔	
v_1, v_2, v_3 (m/s)	0	✔	
$f_1^0;f_2^0;f_3^0$(m)	0.1	✔	
h_1^0(m)	8.6		✔
h_2^0(m)	5.0		✔
h_3^0(m)	4.15		✔
$k_{\min}$(m/day)	$7.9 \cdot 10^{-7}$		✔
λ (−)	1		✔
n (−)	1		✔
η/z (kPa s m^{-1})	$2 \cdot 10^7$		✔
D (m^2/year)	700		✔
φ' (°)	13.7		✔

behaviour [3, 19, 23, 28]. The parameters used in the simulations are detailed in Table 1 (single–block case) and Table 2 (compound rockslide). Table 3 shows the calibrated parameters for the Piagneto rockslide.

3.1 Single block sliding

3.1.1 Influence of the fracture permeability

This section reports on the performance of the model when considering the sliding of a single block isolated from the rock mass. The landslide configuration follows the scheme depicted in Fig. 1a, for the block 1 only.

The first analysis (Case 1 in Table 1) focuses on the influence of changes in water column height within the fracture on the progression of movement. The system has an initial safety factor of 1.057 for an initial water level in the fracture $h_1^0 = 0.8$ m. The water pressure at the toe of the block is always zero (equivalent to $h_2 = 0$).

The block response to an infiltration of 20 mm/day for 30 days is shown in Fig. 3 for different values of initial fracture permeabilities ($k_{min} = 1 \cdot 10^{-4}$, $5 \cdot 10^{-4}$, and $1 \cdot 10^{-3}$ - m/day; $\lambda = 1$; $n = 1$), assumed for a fracture system with spacing of a few metres and openings on the order of a centimetre [12]. Figure 3 depicts the temporal evolution of

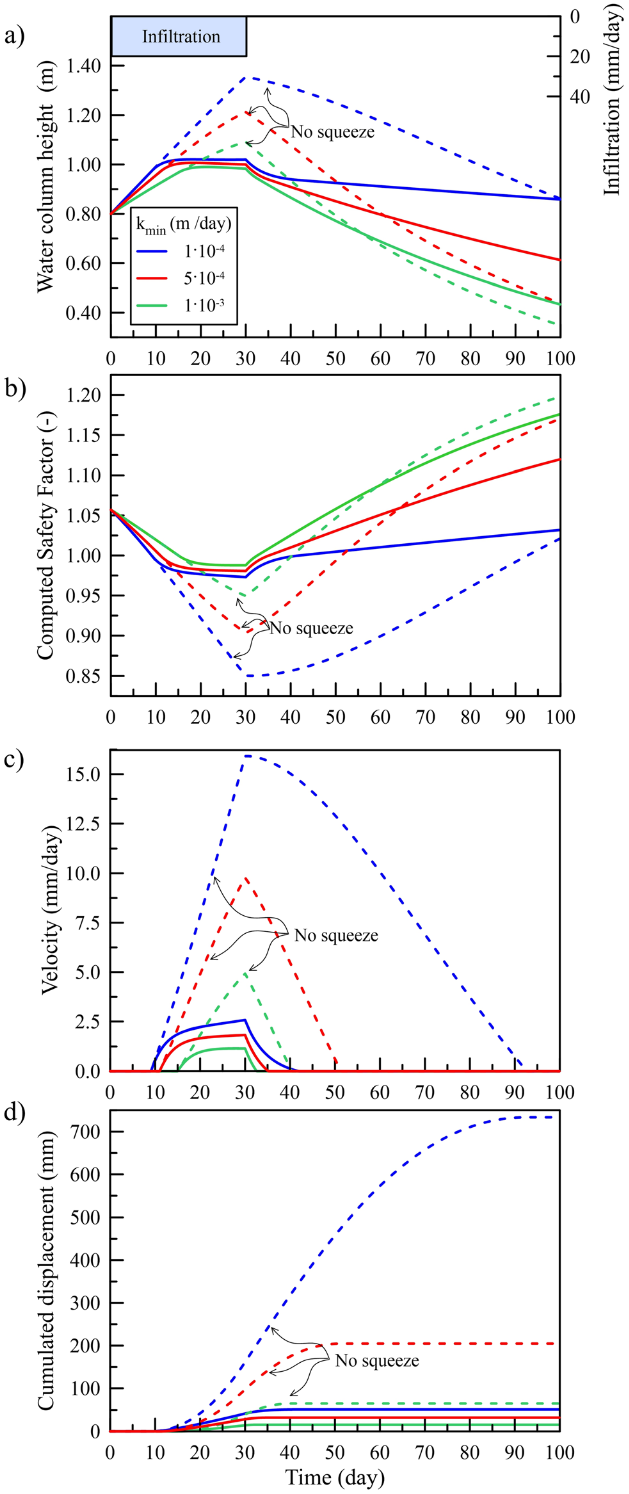

Fig. 3 Single block, case 1: evolution of the water column height in the fracture (**a**), safety factor (**b**), block velocity (**c**) and block displacement (**d**) as a function of the time, for three different values of the fracture permeability. Dotted lines depict the simulations which neglect the negative water-squeezing effect induced by the block movement

the water column height, the computed safety factor, the block velocity, and the cumulated displacement.

The modelling outcomes are presented, distinguishing between scenarios considering the water-squeezing effect (solid lines) and those neglecting it (dashed lines). When the water-squeezing effect is considered, three distinct stages emerge. The initial stage is characterised by an increasing water column in response to infiltration (Fig. 3a) and a reducing safety factor trend (Fig. 3b), culminating in failure conditions ($F = 1$).

During this phase, both the rate of the water column rise and time to failure decrease with increasing fracture permeability. Notably, fracture permeabilities exceeding $2.5 \cdot 10^{-2}$ m/day prevent the water level in the column rise, ensuring block stability. The second stage spans from the time of failure until the conclusion of the infiltration period. During this phase, the block exhibits an increasing velocity and a relatively constant water column.

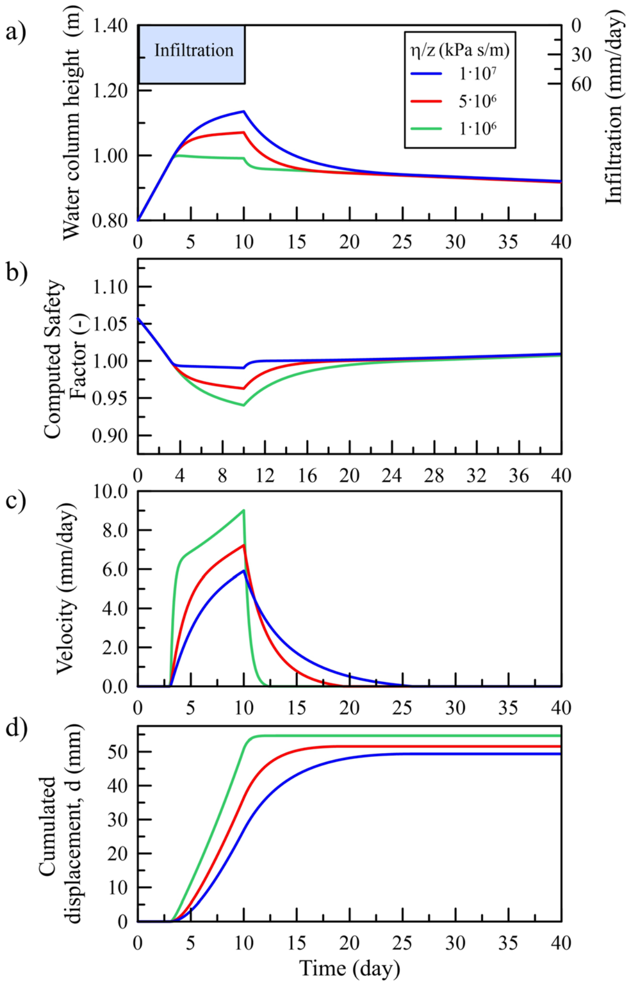

Fig. 4 Single block, case 2a: evolution of the water column height in the fracture (**a**), safety factor (**b**), block velocity (**c**) and block displacement (**d**) as a function of the time, for different values of the viscosity

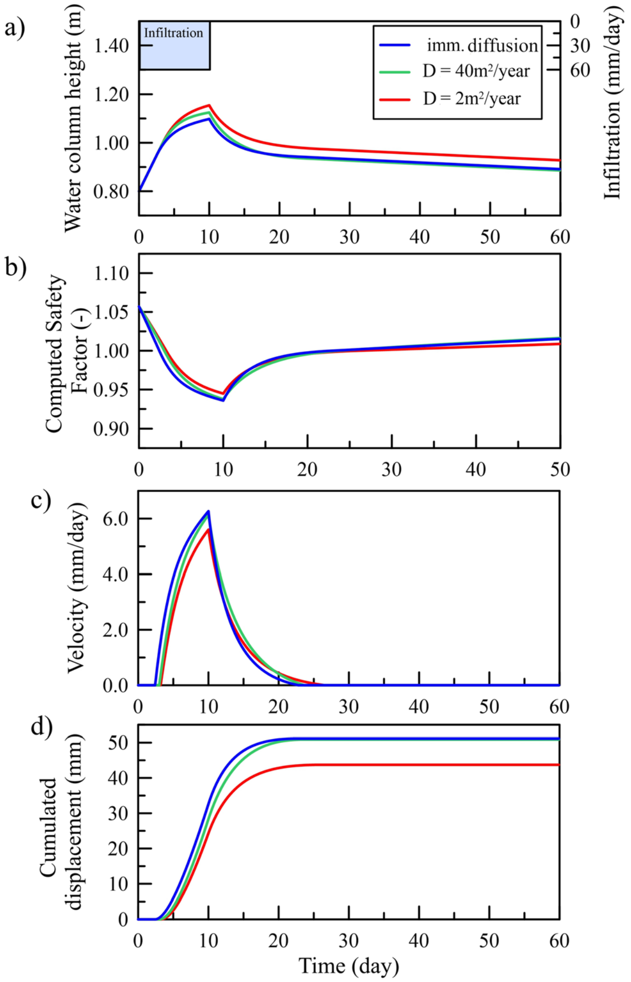

Fig. 5 Single block, case 2b: evolution of the water column in the fracture (**a**), safety factor (**b**), block velocity (**c**) and block displacement (**d**) as a function of the time, for different values of the diffusion coefficient

The maximum velocity, attained at the end of the infiltration, varies with the fracture permeability (Fig. 3c). Lower fracture permeabilities correlate with higher block velocities and cumulative displacements.

The velocity's upward trend is constrained by the development of the viscous force and by the progressive displacement of the block which diminishes the water column in the head fracture (negative squeezing effect). The third stage initiates the post-infiltration phase, wherein the block decelerates until coming to a rest.

3.1.2 Influence of the basal joint hydro-mechanical parameters

The kinematics of the block, characterised by the geometry studied in case 1, is now investigated to assess the influence of viscosity (case 2a in Table 1). The infiltration scenario in this case was varied (q = 60 mm/day and d_i = 10 days)

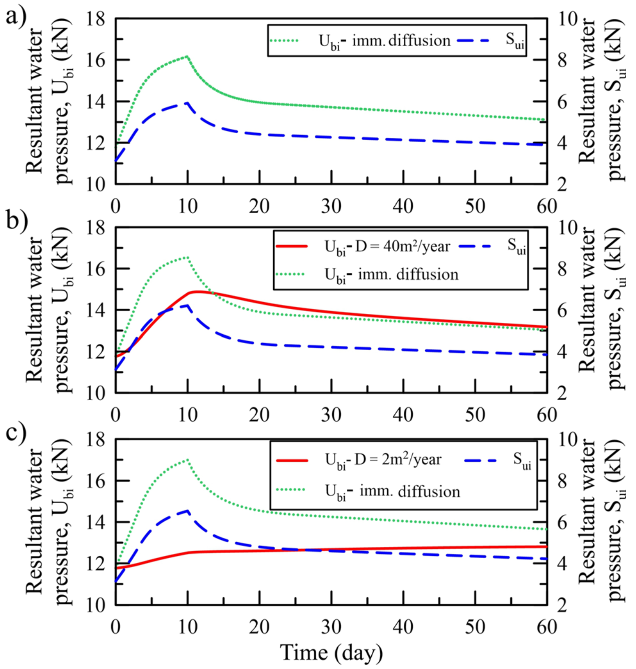

Fig. 6 Single block, case 2b: evolution of the resultant force of water pressure distributions in the fracture S_{ui} and at the base of the block U_{bi} for the immediate diffusion of the water pressure (**a**) for $D = 40$ m^2/year (**b**) and $D = 2$ m^2/year water (**c**). The corresponding evolution of the resultant force at the base U_{bi} for the immediate diffusion is also depicted in b) and c)

while viscosity over thickness ranged between $1 \cdot 10^6$ and $1 \cdot 10^7$ kPa s/m. The obtained results are presented in Fig. 4. As expected, the viscosity is relevant in the post-triggering phase only, with the safety factor increasing more rapidly with increasing viscosity. During the acceleration stage, lower velocities are computed for higher viscosities, while during deceleration, this trend is reversed, leading to an increased duration of the block motion with higher viscosity. Slightly greater displacements were computed for the lowest viscosity value (Fig. 4d).

Figure 5 presents the outcomes of case 2b, in which the role of the diffusion coefficient is explored. Three cases are considered: *i)* immediate diffusion, characterised by instantaneous diffusion of water pressure from the fractures to the base, as in the case of a sandy soil; *ii)* moderate diffusion rate, as in the case of silty-clayey materials ($D = 40$ m^2/year); *iii)* poor diffusion rate, as in the case of clay with very low diffusion coefficient ($D = 2$ m^2/year). As shown, the lowest diffusion properties result in a slightly delayed response of the block, which is closely dependent on the long-term changes in the water level inside the fracture, and a reduction in the cumulated displacement.

The delayed response of the block is further shown in Fig. 6, where the evolutions of the resultant forces of water pressure distributions at the base (U_{bi}) and in the fracture (S_{ui}) are depicted. This representation highlights that the reduction in the diffusion properties induces a slight asynchrony in the forces acting in the fracture and at the base. For larger blocks the effects of the diffusion properties can be more significant (see Sect. 3.3).

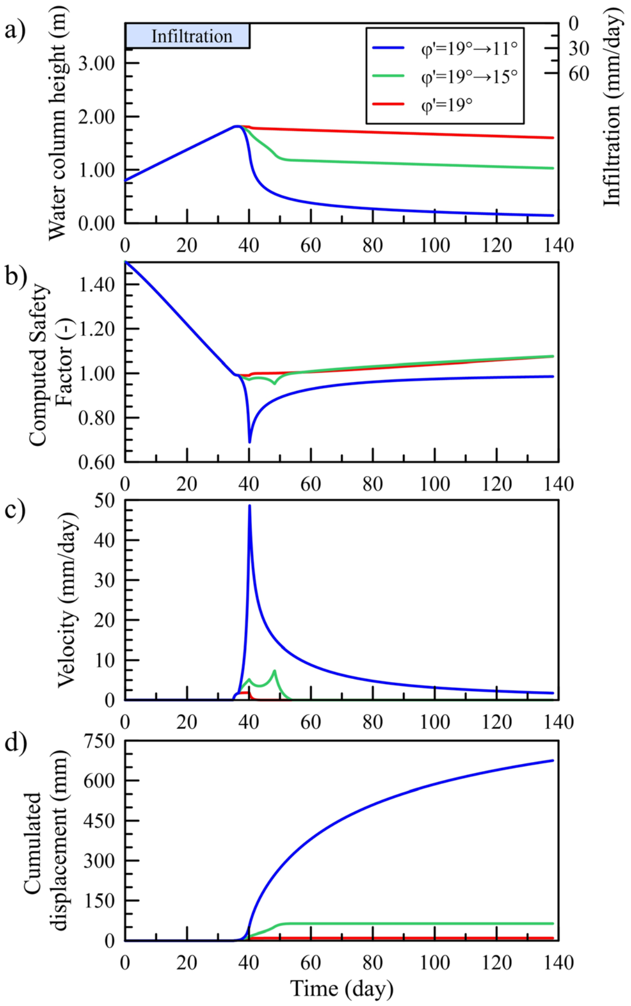

Fig. 7 Single block, case 2c: evolution of the water column in the fracture (**a**), safety factor (**b**), block velocity (**c**) and block displacement (**d**) as a function of the time, for different residual strength parameters

The simulations were also replicated by introducing a shear strength angle at the base dependent on the cumulative displacement. Specifically: *i)* a peak shear strength angle was maintained up to 2 mm of displacement; *ii)* a constant residual shear strength angle was retained after 50 mm of displacement; *iii)* a shear strength angle linearly decreasing between 2 and 50 mm was accounted for. In the simulations, the peak shear strength angle was set at 19°, while the residual shear strength angle φ_r' varied between 11°, 15° and 19° (i.e. an absence of strain-softening behaviour in the latter case). For an applied infiltration of $q = 30$ mm/day, the block starts to move after 35 days.

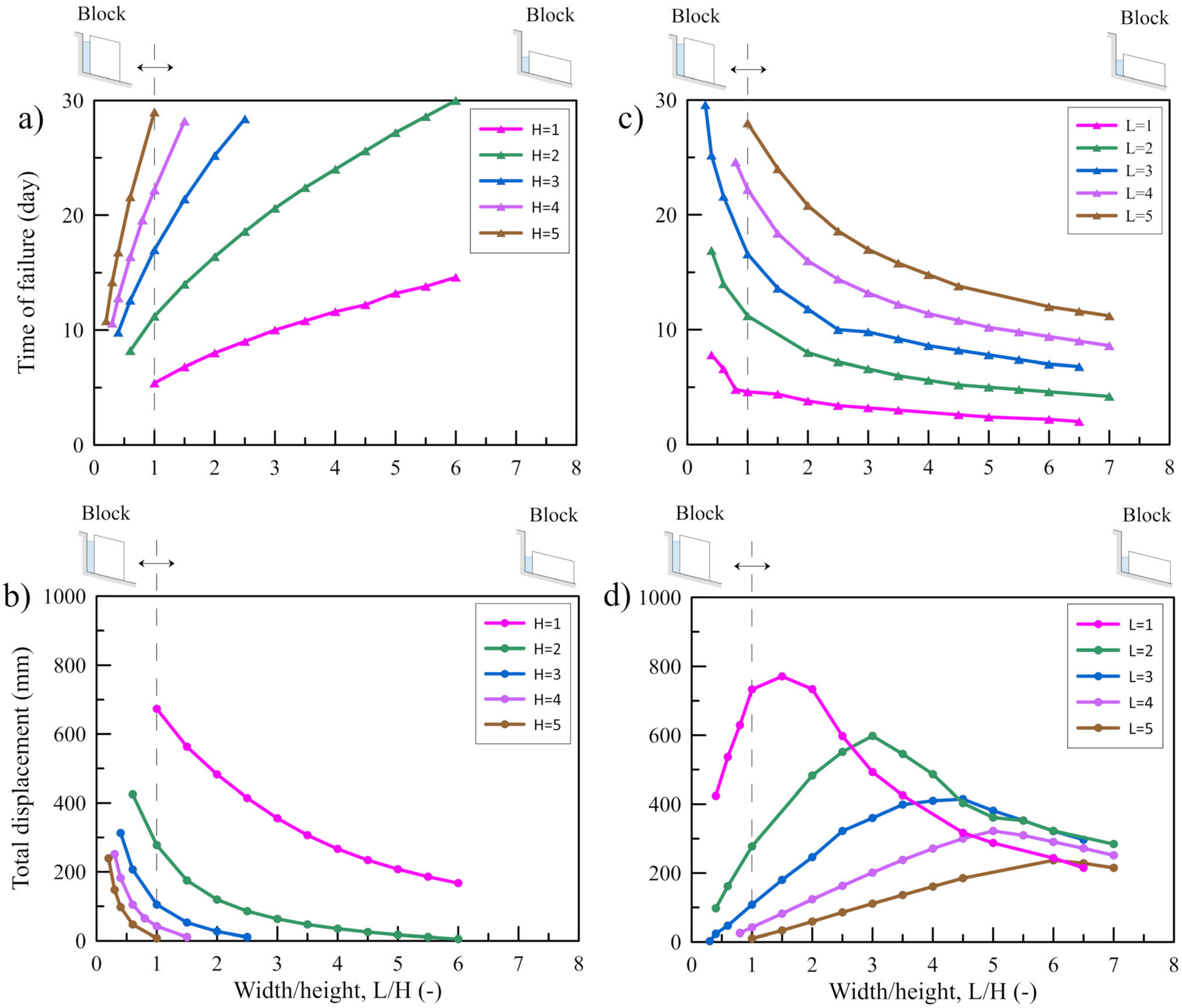

Fig. 8 Comparative analysis between different geometric configurations in terms of time of failure (**a** and **c**) and total displacement (**b** and **d**) of the blocks. In **a**) and **b**) *H* is fixed whereas in **c**) and **d**) *L* is assumed as a constant parameter for each curve

The results depicted in Fig. 7 reveal that the progression of movements significantly varies based on the evolution of the shear strength angle with the cumulated displacement. Despite a pronounced reduction in the water column within the fracture post-triggering, the lowest residual strength angle induces a rapid, nonlinear acceleration in velocity and a continuous movement of the block until the end of the simulation. It is noteworthy that the initial sub-vertical trend of the velocity observed in this case is consistent with that usually observed in first-time landslides characterised by a brittle behaviour. However, it should be noted that the model does not consider the generation of excess of pore pressure that can be relevant in the undrained response involved in first-time failures.

3.1.3 Influence of the block geometry

A comparative analysis of different geometric configurations was carried out to assess the influence of shape on the kinematic behaviour of the block. The shape of the block is delineated by the *L/H* ratio. If the width is large and the height is relatively small, the block is considered as a "*slab*". Conversely, if the width is less than the height, the block assumes a "*columnar*" shape. In the assumed 2D modelling approach, the thickness of the block is consistently assumed to be unitary.

The simulations were conducted in two sets. Initially (case 3a in Table 1 and Fig. 8a, b), the height (*H*) was maintained as a constant, while the *L/H* ratio was varied from 0.2 to 7. Subsequently (case 3b in Table 1 and Fig. 8c, d), the width (*L*) was set as a constant, and the *L/H* ratio was varied within the same range of values. Hydraulic and geotechnical parameters were held constant and are listed in Table 1. In order to maintain comparability across cases with varying dimensions, the initial hydraulic conditions (specifically, the water column height in the fracture) were selected to ensure that the initial safety factor of the block was consistently equal to 1.05. Infiltration conditions were set at $q = 40$ mm/day with $d_i = 30$ days.

Figure 8 shows the variations of the time of failure (Fig. 8a, c) and the overall block displacement (Fig. 8b, d) in relation to *L/H*.

In the case 3a, Fig. 8a, b demonstrates that blocks with lower heights (*H*) exhibit greater instability, evidenced by shorter times of failure and higher cumulative total displacements. Conversely, when *H* is fixed, blocks with higher *L/H* ratios demonstrate increased stability. This is attributed to the increased mass of the block, which requires more water storage in the fracture to reach failure conditions. Additionally, the linear increase in viscous force at the base of the block with *L* further constrains the total displacement. Figure 8c, d shows that curves with fixed *L* exhibit upward concavity. Specifically, Fig. 8c demonstrates that, for a constant *L/H* value, increasing *L* extends the time of failure. However, when *L* is held constant and *L/H* is increased, the time of failure reduces. Furthermore, Fig. 8d illustrates that higher *L* values correspond to lower total displacements. Nevertheless, for increasing *L/H* values, the total displacement curves display a peak. This phenomenon is associated with the maximum water column that can be stored in the fracture. In fact, the reduced height of the block causes water to spill over from the top of the fracture, resulting in a constant resultant force of water pressure, even during prolonged infiltration. Consequently, the *L/H* value corresponding to the maximum total displacement increases with *L*. Interestingly, even if the toppling mechanisms are not

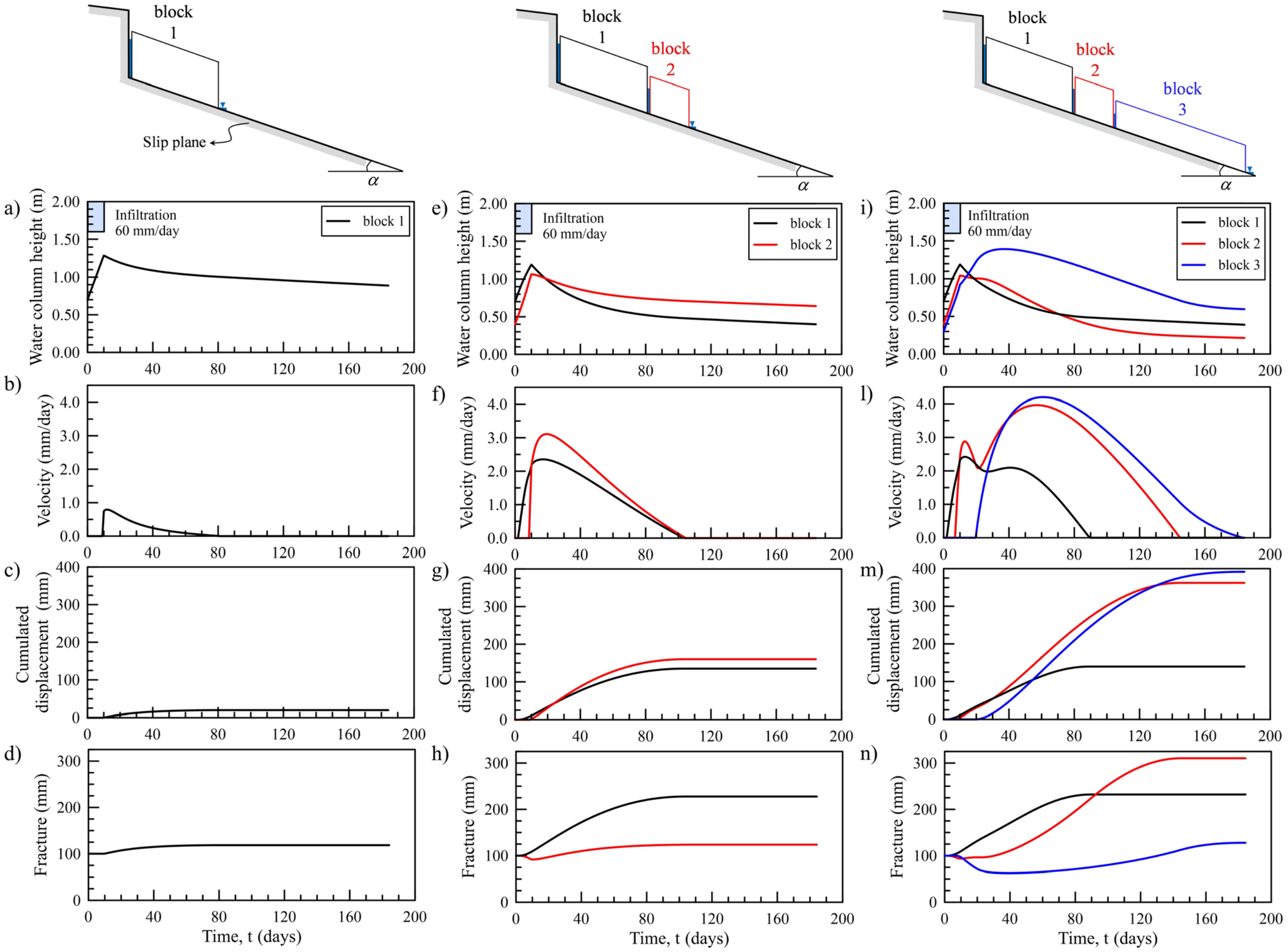

Fig. 9 Simulations carried out with the aim to highlight the interaction mechanism between different blocks: **a**, **b**, **c**, and **d** show the simulation of the behaviour of a single block (case 4a); **e**, **f**, **g**, and **h** show the simulations for a two blocks system (case 4b); **i**, **l**, **m**, and **n** show the behaviour of three blocks (case 4c). The behaviour of the first upward block is depicted by a black line, whereas the second and third downward blocks with a red and blue line, respectively

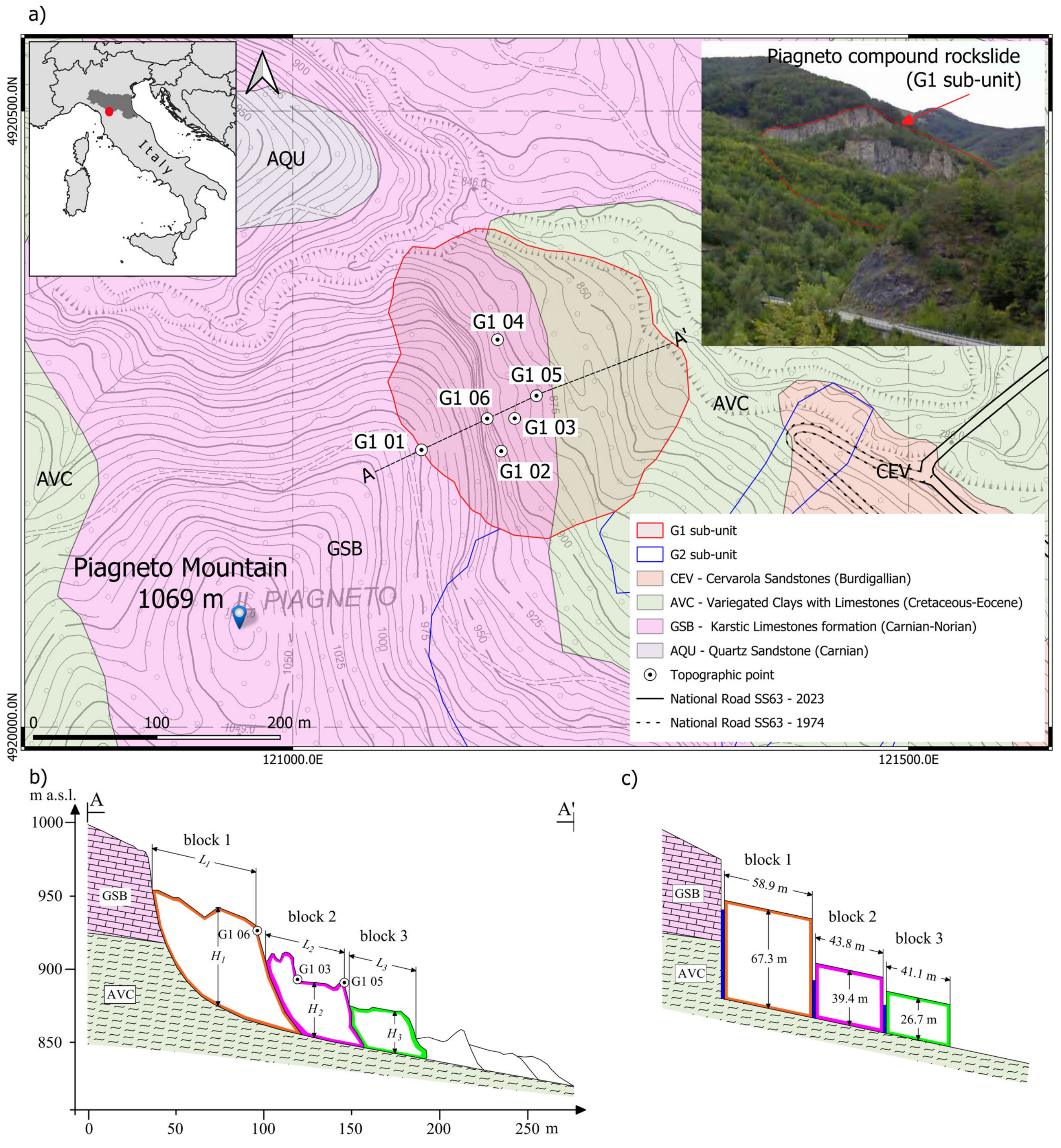

Fig. 10 **a** Localization of the Piagneto rockslide (Reference System WGS84 UTM33N–EPSG:32,633); **b** the real landslide profile; **c** the simplified profile used in the model

considered here, the columnar blocks with narrow bases are more unstable than the long slab blocks.

3.2 Compound sliding

To highlight the interaction mechanism among diverse blocks and offer a more comprehensive understanding of the role of water within the fractures separating the blocks, the results of three distinct simulations are reported in Fig. 9. The simulation parameters are detailed in Table 2. The first case under examination involving a single 10 m × 5 m slab block (case 4a) serves as a reference case for the subsequent analyses. Positioned on a clayey subsoil inclined at 19° to the horizontal, the fracture between the block and the stable rear formation experiences infiltration with an intensity of $q = 60$ mm/day for $d_i = 10$ days. As depicted in Fig. 9a, b, the water column within the fracture exhibits a linear increase until the block starts to move. The movement induces the opening of the fracture (Fig. 9c, d). Concurrently, the water column reduces (Fig. 9a) due to the negative water-squeezing effect. The water outflow from the fracture remains negligible owing to its low permeability. Subsequently, the block decelerates, coming to a complete rest before the end of the simulation.

In case 4b, the initial block is accompanied by a second, smaller block positioned downward, with dimensions of 6 m × 4 m and an initial aperture of 100 mm in the fracture between the blocks. Illustrated in Fig. 9e–h, the presence of the second block proves to be fundamental in the overall sliding movement of the system. The second fracture has the capacity to retain the infiltrated water (Fig. 9e) and contributes to increasing the resultant water pressure force (U_{b1}) at the base of block 1. However, over time, the water level in the second fracture experiences fluctuations during the infiltration period and decreases due to the relative movements of the two blocks, indicative of a negative water-squeezing effect. Block 1 starts movement before block 2. Due to the interaction between the blocks, block 1 moves earlier in case 4b compared to case 4a, and it also attains a higher maximum velocity in case 4b than in case 4a. However, block 2 has a maximum velocity higher than block 1. Both block 1 and block 2 come to a simultaneous stop, accumulating different displacements. Fracture 1, located between the first block and the rear stable formation, widens continuously. Meanwhile, the second fracture, which lies between the blocks, undergoes initial closure and subsequently opens as a result of the concurrent movements of the blocks. Therefore, both fractures exhibit distinct behaviours in response to the surrounding block movements.

In case 4c, the simulation explores the case of three blocks, by considering an additional block measuring 15 m in length and 3 m in height. The results are depicted in Fig. 9i–n. While the total displacement of block 1 exhibits minimal variation compared to the previous case, its velocity distribution over time appears somewhat different; its velocity reaches a maximum value as in the case 4b, with a second increasing trend commencing later and culminating in a new peak value of lower intensity. This renewed trend is attributed to the sliding mechanism of block 3, triggered later. Block's triggering also influences the second increasing trend of block 2, elevating its velocity in the second stage of triggering. The overall maximum velocity within the system is achieved by block 3. Notably, despite being the last to be triggered, block 3 undergoes a total displacement greater than the displacement calculated for block 2. In general, fractures between blocks exhibit significant closure and opening sequences due to the relative displacements of the blocks (Fig. 9n).

The analysed case with the three blocks shows the ability of the model to reproduce an advancing sliding mechanism. As illustrated in Fig. 9l, the sequence of movement initiates from the upstream block and progressively involves the downward blocks. Similarly, block 1 is the first to come to a stop, while block 3 is the last. Different phases of movement are associated with the triggering of the sliding of distinct blocks, with the intensity of displacement increasing from the block at the toe of the slope to the one situated at the head of the slope. Nevertheless, through variations in modelling parameters, hydraulic variables, and rainfall scenarios, it is possible to activate different displacement evolutions of blocks within the system, such as a retrogressive landslide mechanism.

3.3 The Piagneto compound rockslide

Located in the Emilian Apennines, close to the border between the Emilia Romagna and Liguria regions (Italy), the Piagneto landslide (Fig. 10a) can be classified as a compound rockslide [27]. From a geological point of view, the mechanism of movement involves a sliding of Triassic limestones (GSB – Karstic Limestones formation) over Oligocene–Miocene clay shale (AVC, Variegated Clays with Limestones formation). In detail, Corsini et al. [6] and Corsini et al. [7] identified two compound rockslides named G1 sub-unit and G2 sub-unit, sharing the same geological and kinematic characteristics (see Fig. 10a).

Analysis of aerial photographs from the last 50 years shows significant changes in the slope, characterised by retrogressive movements of more than 50 m. The active compound rockslide showed seasonal reactivation with varying displacement velocities, depending on the distribution of rainfall. These phenomena induce a high risk for the nearby national road SS63 and its users. In May 1974, the rockslide experienced a failure, burying a 150 m long section of the road. Subsequently, the impaired roadway was forsaken in favour of an alternative path. However, in 2008, the newly constructed road was damaged again, forcing the authorities to rebuild the previously abandoned, damaged 1974 road [6]. Over a period of about 2 and a half years (starting from 29th July 2011 and ending to 4th February 2014), the G1 sub-unit was subjected to systematic monitoring, which included the measurement of both rainfall intensities and displacements [8]. The cumulative rainfall was recorded using a weather station, while the displacements were quantified utilising the Automated Total Station (ATS) method, leveraging topographic control points (ATS prisms) strategically positioned on the rockslide (see Fig. 10a). The monitoring measurements provided evidence of the landslide mechanism, where large

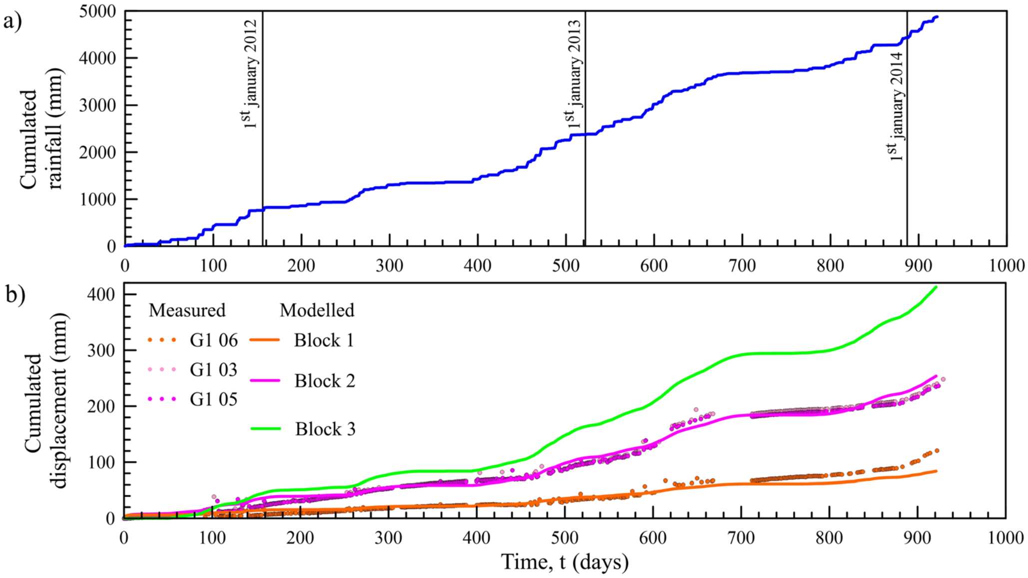

Fig. 11 Cumulative rainfall referred to the Piagneto area in the period 24 July 2011 – 4 February 2014 (**a**) and comparison between the measured and modelled displacement of the G1 sub-unit blocks (**b**)

and tall rock blocks rigidly slide, with a negligible rotational component [6]. Rainwater infiltration in the fractures between the rigid blocks was assessed as the cause of the ground instability. The shear failure was localised at the interface between the clayey substratum and the rock blocks (Fig. 10b). No information was available about the water level in the fractures and the thickness of the shear bands, due to the significant depth of the sliding surface and the difficulty in performing observations.

The compound rockslide G1 sub-unit is approximately 250 m in length, 230 m in width, and encompasses a volume of about $2.5 \cdot 10^6$ m^3 [6]. It shows similar characteristics to the ones considered in the model introduced in this paper. As shown in Fig. 10c, the landslide body can be schematised as a sequence of a prismatic blocks, each with the same mass as the corresponding real block. Based on the data monitoring, a calibration procedure was implemented to obtain the model parameters, to evaluate the model's performance and provide a critical interpretation of the observed behaviour of the Piagneto rockslide. The calibration procedure was based on the best fit of the modelled displacement to the measured displacements of the blocks; for the measured ones, the projection of the absolute displacement of the topographic control points onto the direction of the slope was considered. In the adopted procedure, some parameters were assessed on the basis of the geometry and physical characteristics of the blocks (e.g., height, length, unit weight of the blocks and the initial aperture of the fractures) while the others were calibrated by minimising the sum of the quadratic errors of block 1 and block 2's displacements in comparison to topographic points G1 06 and G1 05, respectively (Fig. 10a, b). The shear strength angle at the interface *φ'* is assumed to be constant and the same for all the considered blocks. It can be considered as a residual strength parameter, in consideration of the fact that the landslide is reactivated.

The viscosity parameter was calibrated per unit thickness of the shear band (η/z), as is typically considered in slow-moving landslide modelling when adopting viscous approaches [1, 5, 17, 31]. This choice is justified by Van Asch et al. [31] due to the difficulties in predicting the actual viscosity value within the shear band from laboratory tests, the complexity of identifying viscous movements in the broader zone surrounding the discrete shear band, and the influence of dilatancy effects associated with the wavy shape of the slip surface at the local scale. The value of permeability coefficient resulting from the back-analysis procedure is consistent with the geometry of the fractured rock mass in the landslide body, which is characterised by tall blocks separated by pre-existing open fractures with very large spacing, on the order of tens of meters.

The initial height of the water column in the fractures was also determined through the calibration procedure. In particular, an algorithm based on the generalized reduced gradient (GRG) method was used, with the sum of the squared displacement errors adopted as the objective function. The optimal solution was considered achieved when, as the calibration parameters were adjusted at each computation step, the gradient of the objective function approached zero. The parameters obtained with the procedure applied to the Piagneto rockslide are listed in Table 3.

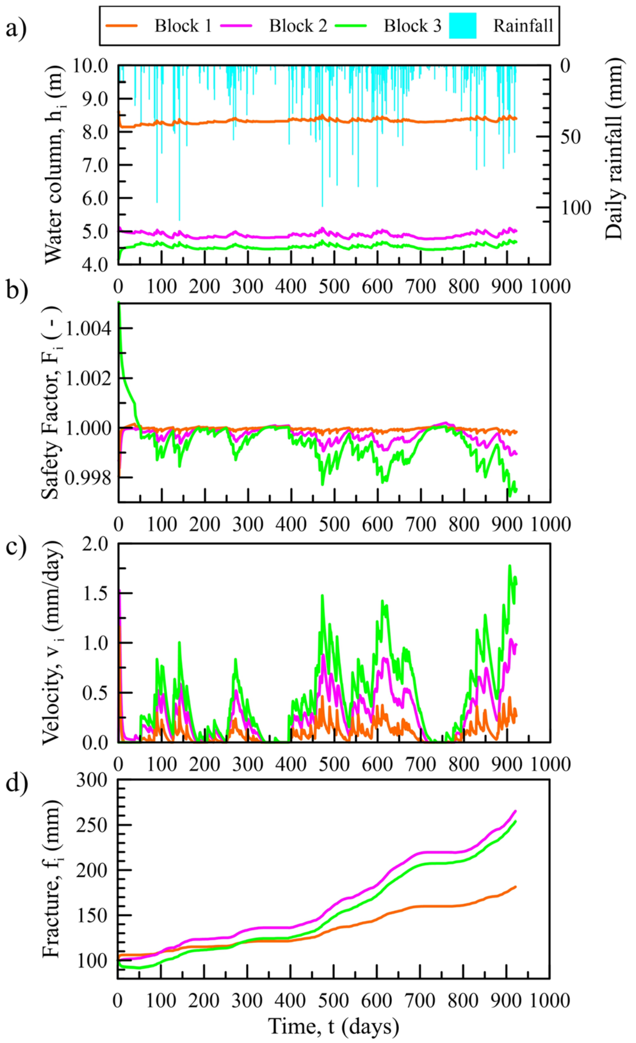

Fig. 12 Results of the Piagneto rockslide modelling in terms of water column height within the fractures (**a**), safety factor (**b**), velocities of blocks (**c**) and aperture of the fracture (**d**) over time. In a) the daily rainfalls are also depicted

Figure 11a depicts the cumulative rainfall in the Piagneto landslide area, with a total cumulative rainfall for the monitoring period equal to 4900 mm. Figure 11b shows the evolution over time of the measured and the modelled displacements of the blocks. By comparing Fig. 11a, b, it is possible to observe that for each increment in the cumulative rainfall, there is a corresponding increase in the block displacements. The comparison between the curves relative to the same blocks (G1 06 for bock 1; G1 05 and G1 03 for block 2) proves that the model can capture both the time of the different reactivations of the movement and, with good accuracy, the final displacement of the blocks. For block 3, for which unfortunately displacements were not measured, the model predicts the largest displacements.

Figure 12 shows the computed temporal variations in the water column height within the fractures (Fig. 12a), the safety factor (Fig. 12b), the velocity of the blocks (Fig. 12c), and the aperture of fractures among the blocks (Fig. 12d).

As shown in Fig. 11b, the water column heights exhibited a decreasing trend from block 1 to block 3. Limited fluctuations in the quasi-stationary water column values were calculated during the rainy periods (Fig. 12a). Despite their relatively modest magnitude, these variations play crucial role in the triggering of the block movements. Notably, the safety factors for the three blocks exhibited a narrow range of variation throughout the modelling period, ranging between 0.997 and 1.005 (Fig. 12b). However, the movements of the blocks are not directly correlated with the single daily rainfall event. In fact, it is easy to highlight in Fig. 12c that the highest block velocities do not correspond with the most important daily rainfall events. This departure from intuitive expectations is ascribed to the influence of the temporal diffusion of water pressure at the base of the blocks on their stability. The blocks underwent six distinct stages of movement, each featuring a peak velocity. Notably, block 3 exhibited higher velocities, reaching up to a maximum of 1.7 mm per day, in comparison to the other blocks. In contrast, block 1 consistently displayed lower velocities, peaking at a maximum of 0.5 mm per day. The consequential gaps in block velocities play a role in driving variations in the apertures of fractures, as delineated in Fig. 12d. These have a significant impact on the fluctuation of the water level within the fractures, due to the water-squeezing effect. It is worth noting that the negative water squeezing effect can be considered as an indispensable tool in modelling the Piagneto composite landslide, particularly due the low permeability of the fractures determined by the calibration procedure (see Table 3).

4 Conclusions

This paper introduced a new model to analyse the behaviour of compound rockslides. The model incorporates key features of the sliding phenomenon, encompassing the effects of water stored in fractures, viscosity impact on the sliding surface, and the delayed temporal diffusion of water pressure at the base of the blocks. Additionally, the water-squeezing effect is employed to simulate the interaction between non-contacting adjacent blocks, where discontinuities are fully open. This model integrates stability analysis preceding failure and subsequent movement simulation of the landslide body over time within a unified hydro-mechanical framework.

A sensitivity analysis was carried out in order to explore the fundamental role of open vertical fractures, focusing on permeability and water-squeezing effects, as well as basal joint hydro-mechanical parameters (viscosity, diffusion coefficient, and strength interface), and block geometry. A total of 125 simulations across nine scenarios, encompassing both simplified single-block and multi-block systems on inclined slopes, were presented with the aim of evaluating the influence of variation in model parameters. Finally, the model has been applied to a real case study of a rockslide located in Piagneto (Italy). This simulation served to calibrate the proposed model, demonstrating its ability to successfully capture and represent the kinematic, hydraulic, and mechanical characteristics of this compound landslide. The model was developed in a two-dimensional framework, which simplifies the geometry of rockslides. Extending the approach to three dimensions would require an explicit representation of fracture networks and their hydraulic connectivity, together with more complex block interactions, leading to a substantial increase in model complexity. Despite this simplification, the results show that the 2D formulation captures the main hydro-mechanical processes controlling the behaviour of slow-moving compound rockslides.

The model emerges as a promising tool for realistically simulating and predicting rockslide behaviour, offering insights into triggering mechanisms and post-failure displacement evolution under diverse hydro-mechanical and climatic conditions. In spite of the fact the model has been here used in synthetic cases and for a real landslide for which not all needed monitoring data were available (e.g. the real water levels in the fractures), it has been shown that accounting for the evolution of the water levels within the fractures is an important factor to interpret the displacement trends of different blocks. Thus, the model offers a valuable assessment of key hydro-mechanical parameters that govern these complex phenomena and may serve as a useful tool to guide further field investigations, particularly in contexts where direct measurements remain challenging.

Appendix A Computation of the water pressure at the base of the blocks.

The schematic depiction of the diffusion process beneath the block is illustrated in Fig. 13. The diffusion process is considered to be one-dimensional along the block base L_i and it is governed by the following equation:

$$\partial u_e/\partial t = D \cdot \partial^2 u_e/\partial y_j^2 \tag{12}$$

where u_e is the excess water pressure, D is the diffusion coefficient and y_i is the distance from the left edge of the block, which varies between 0 and L_i. The diffusion coefficient D is treated as an operational parameter to be determined through back-analysis. As depicted in Fig. 13, the top and bottom surfaces of the narrow band are treated as impermeable, with hydraulic boundary conditions imposed by water pressure at points P and Q. Simultaneously, vertical fractures serve as left and right free drainages for the diffusion process of the base layer; hence, boundaries at points P and Q are considered permeable. Given that the water pressure in P and Q undergoes changes at each step time, the principle of superposition can be utilised to assess the effect of each variation of the water column height $h_i(t)$ over time [16]. In other words, the diffusion process due to a given variation evolves

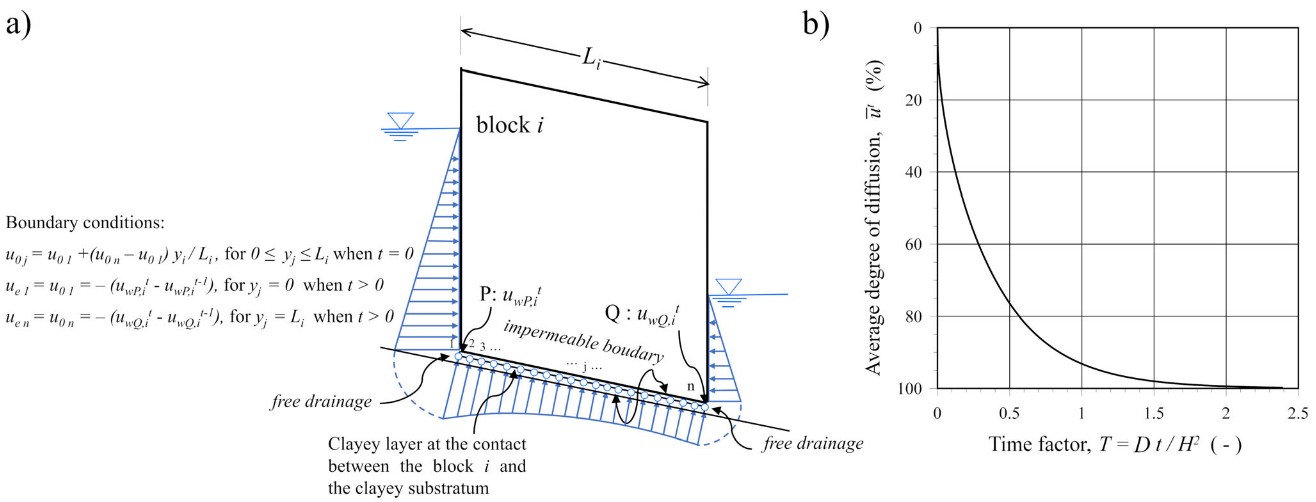

Fig. 13 Boundary conditions for the diffusion process at the bottom surface of the block i. At each time step in which the water pressure at the bottom of the vertical fractures (i.e. at edge $u_{wP,i}$ (t) and $u_{wQ,i}$ (t)) changes, an additional diffusion process can be studied. The evolution of the average degree of diffusion as a function of the time factor obtained by means of finite-difference solution is plotted in b)

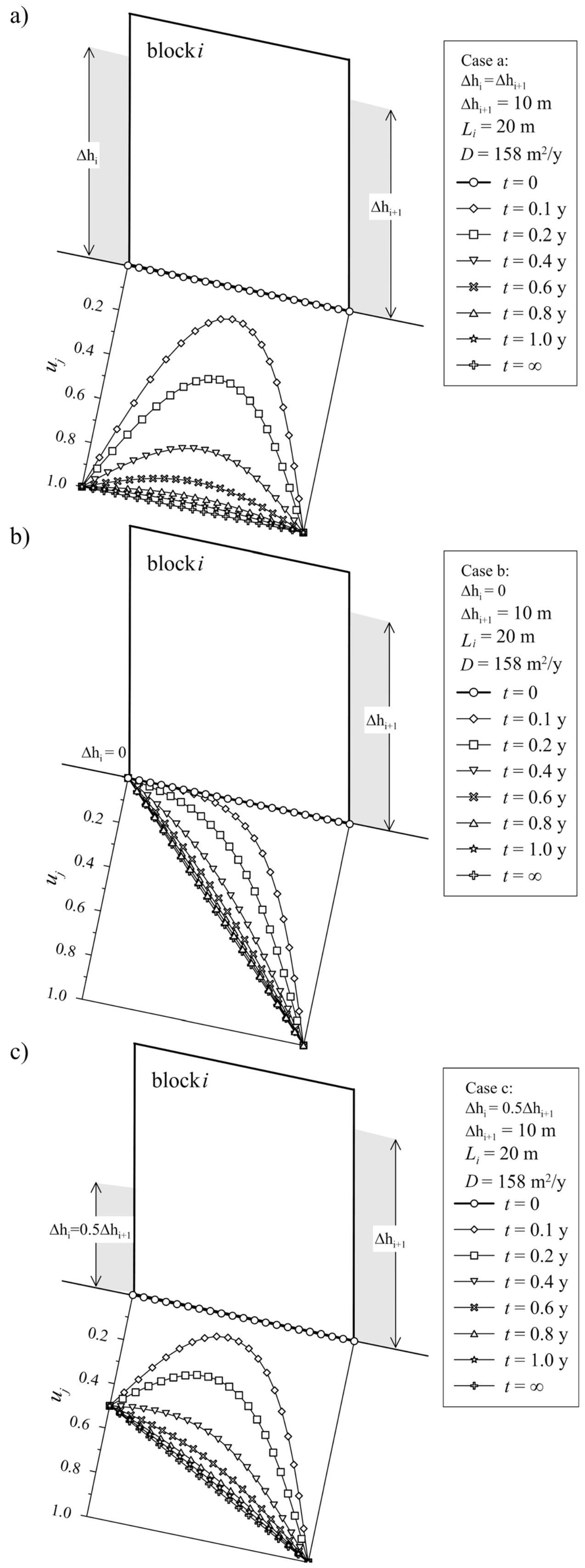

◀**Fig. 14** Evolution with time of the water pressure at the bottom of the block for three different hydraulic boundary condition: rectangular ($\Delta h_i = \Delta h_{i+1}$ = constant, in a), triangular (Δh_i = constant and Δh_{i+1-} = 0, in b) and trapezoidal (Δh_i = constant and $\Delta h_{i+1} = 2\Delta h_i$, in c). Water column height in the vertical joints is assumed as a constant value with time

independently of that due to the previous or subsequent variation.

Equation (13) can be solved by applying the finite difference technique as follows:

$$\left(u_{ej}^{t+1}-u_{ej}^{t}\right)/\Delta t = D\cdot\left(u_{ej+1}^{t}-2u_{ej}^{t}+u_{ej-1}^{t}\right)/(\Delta y_i)^2 \tag{13}$$

and then the excess of pore water pressure u_{ej}^{t+1} at the point j of the mesh in Fig. 13 at the time steps $t+\Delta t$ is equal to:

$$u_{ej}^{t+1}=u_{ej}^{t}+\beta\left(u_{ej+1}^{t}-2u_{ej}^{t}+u_{ej-1}^{t}\right) \tag{14}$$

where the dimensionless parameter $\beta = (D\ \Delta t)/(\Delta y_i)^{2-} \leq 0.5$ to have a stable and convergent numerical solution [10, 18].

Considering that the initial excess of water pressure u_{0j} is:

$$u_{0j}=-\left(u_{wj}^{t=\infty}-u_{wj}^{t=0}\right)=u_{wj}^{t=0}-u_{wj}^{t=\infty} \tag{15}$$

the local degree of diffusion u_j can be classically defined as:

$$u_j = 1-u_{ej}/u_{0j} \tag{16}$$

The numerical method can be easily applied to different types of hydraulic boundary conditions, which are essentially controlled from the water level variation in the fracture (Δh_i and Δh_{i+1} from Fig. 13). For example, in Fig. 14 the evolution of the local degree of diffusion u_j is plotted for the rectangular ($\Delta h_i = \Delta h_{i+1} = 10$ m in Fig. 14a), triangular $\Delta h_i = 10$ m and $\Delta h_{i+1} = 0$ in Fig. 14b) and trapezoidal $\Delta h_i = 0.5$ and $\Delta h_{i+1} = 10$ m in Fig. 14c) changes of water column height. In these cases, the following were assumed: $L_i = 20$ m; $D = 158$ m^2/year; $h_i^0 = h_{i+1}^0 = 0$; heights of water filling the vertical fracture constant with time ($h_i^t = h_{i+1}^t$ = constant for $t > 0$).

These curves were plotted as a function of the time and the time factor $T = D\cdot t/L_i^2$, according to the classical representation of isochrones for the graphical solutions of the Terzaghi equations [24].

The average degree of diffusion $\overline{u}^t$ at each time step Δt can be numerically computed, adopting the Cavaleri–Simpson's rule, as follows:

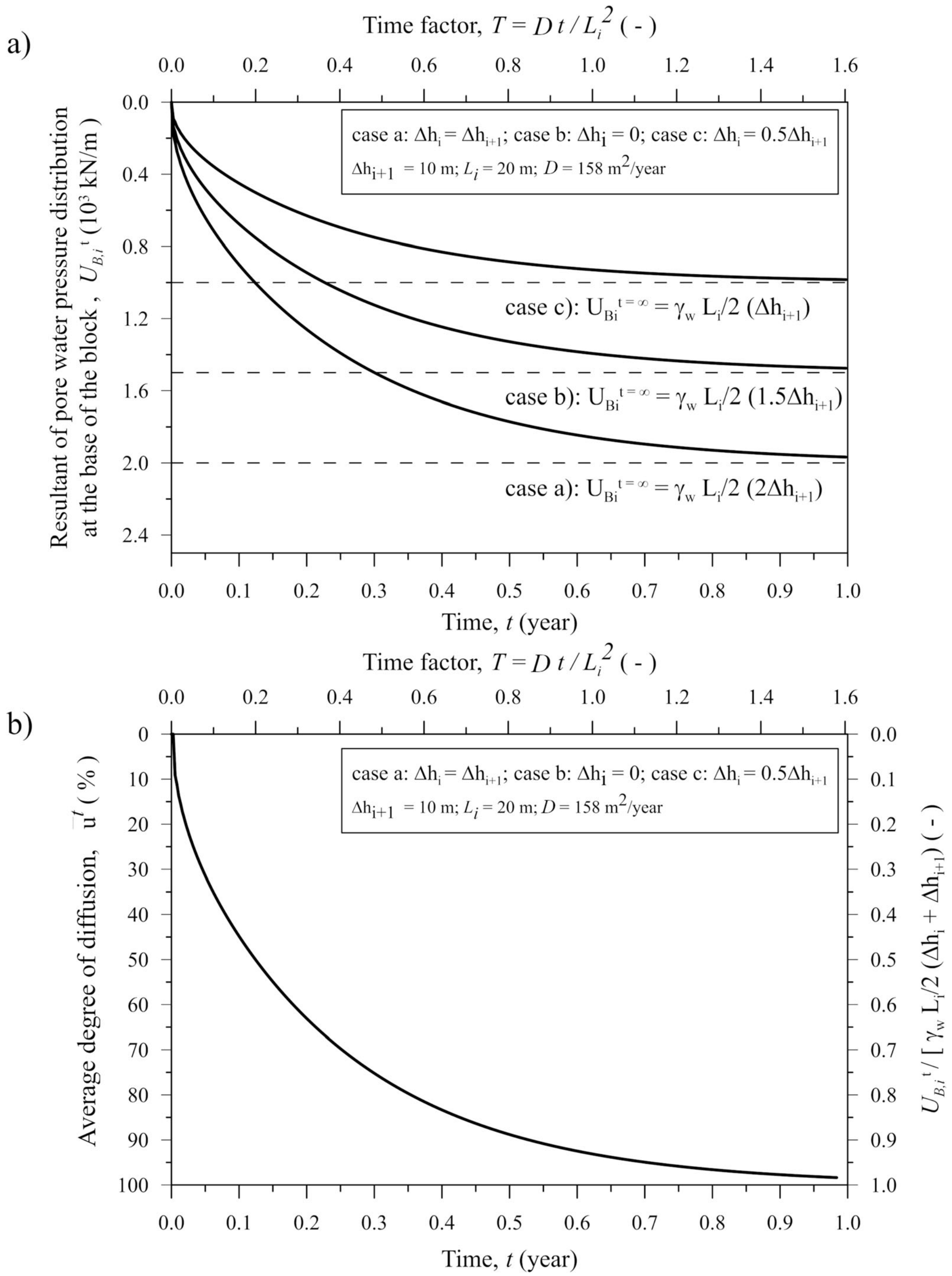

Fig. 15 In **a** evolution with time of the resultant of the water pressure at the bottom of the block for three different hydraulic boundary conditions: rectangular (Δh_i = Δh_{i+1} = constant) triangular (Δh_i = constant and $\Delta h_{i+1} = 0$) and trapezoidal (Δh_i = constant and $\Delta h_{i+1} = 2\Delta h_i$). In **b** the evolution with the time of the average degree of diffusion $\overline{u}^t$ for the rectangular, triangular, and trapezoidal hydraulic conditions (filling water in the vertical joints is assumed as a constant with time) are depicted. In both diagrams, the corresponding time factor axis is reported on the top

$$\bar{u}_t = \int_0^{L_i} \left(u_{0j} - u_{ej}^t\right)\mathrm{d}y / \int_0^{L_i} u_{0j}\mathrm{d}y = 1 - \int_0^{L_i} u_{ej}^t\mathrm{d}y / \int_0^{L_i} u_{0j}\mathrm{d}y$$
$$\approx 1 - \Delta y/3\left(u_{e0}^t + 4u_{e1}^t + 2u_{e2}^t + \ldots + 4u_{en-1}^t + u_{en}^t\right)/$$
$$- \int_0^{L_i} \left(u_{wj}^{t=\infty} - u_{wj}^{t=0}\right)\mathrm{d}y \tag{17}$$

The evolution of $\overline{u}^t$ with the time factor $T = D \cdot t/H^2$ is plotted in Fig. 13b. Again, the average degree of diffusion $\overline{u}^t$ can be related to ΔU_{bi}^{t}(i.e. the change in the resultant of the water pressure distribution at the base of block) at the instance t considering that:

$$\overline{u}^t = \int_0^{L_i} \left(u_0 - u_e^t\right)\mathrm{d}y / \int_0^{L_i} u_0\mathrm{d}y$$
$$= - \int_0^{L_i} \left(u_0 u_z^t\right)\mathrm{d}y / \int_0^{L_i} \left(u_{wj}^{t=\infty} - u_{wj}^{t=0}\right)\mathrm{d}y$$
$$= \int_0^{L_i} \Delta u_{wj}^t\mathrm{d}y / \int_0^{L_i} \left(u_{wj}^{t=\infty} - u_{wj}^{t=0}\right)\mathrm{d}y = \Delta U_{bi}^t / \Delta U_{bi}^{t=\infty} \tag{18}$$

Subsequently, knowing the average degree of diffusion $\overline{u}^t$, the variation in the resultant pore water pressure distribution at the base of the i-th block *i-th* ΔU_{bi}^{t}, for a variation of water pressure along the fracture can be computed as follows:

$$\Delta U_{bi}^{t} = \overline{u}_t\, \Delta U_{bi}^{t=\infty} \tag{19}$$

Applying the superposition principle, the resultant pore water pressure at the base of the block *i-th* U_{bi}^t corresponding to a sequence of changes in water pressure along the fractures at the computation time t can also be obtained as:

$$U_{bi}^{t_c} = \left(u_{wPi}^0 + u_{wQi}^0\right)L_i/2$$
$$+ \sum_{t=1}^{t_c} \left[\left(u_{wPi}^t - u_{wPi}^{t-1}\right) + \left(u_{wQi}^t - u_{wQi}^{t-1}\right)\right](L_i/2)\overline{u}^{t_c - t} \tag{20}$$

moreover, considering the heights of the water filling the fracture h_i and h_{i+1} and their variation $\Delta h_i^{t,t-1}$ and $\Delta h_i^{t,t-1}$ in the time step Δt:

$$U_{bi}^{t_c} = \gamma_w L_i/2\left[\left(h_i^0 + h_{i+1}^0\right) + \sum_{t=1}^{t_c}\left(\Delta h_i^{t,t-1} + \Delta h_{i+1}^{t,t-1}\right)\overline{u}^{t_c - t}\right] \tag{21}$$

Figure 15 depicts the temporal evolution of the average degree of diffusion $\overline{u}^t$ for the rectangular, triangular, and trapezoidal conditions (Fig. 14a–c). As shown the trend of $\overline{u}^t$ is unique for the three different conditions simulated. Furthermore, in accordance with equation (21), the temporal evolution of the factor $U_{bi}^t/[\gamma_w\ L_i\ /2\ (\Delta h_i + \Delta h_{i+1})]$ (i.e. the ratio between the resultant of the water pressure distribution at the base of block at the time t and the resultant of the water

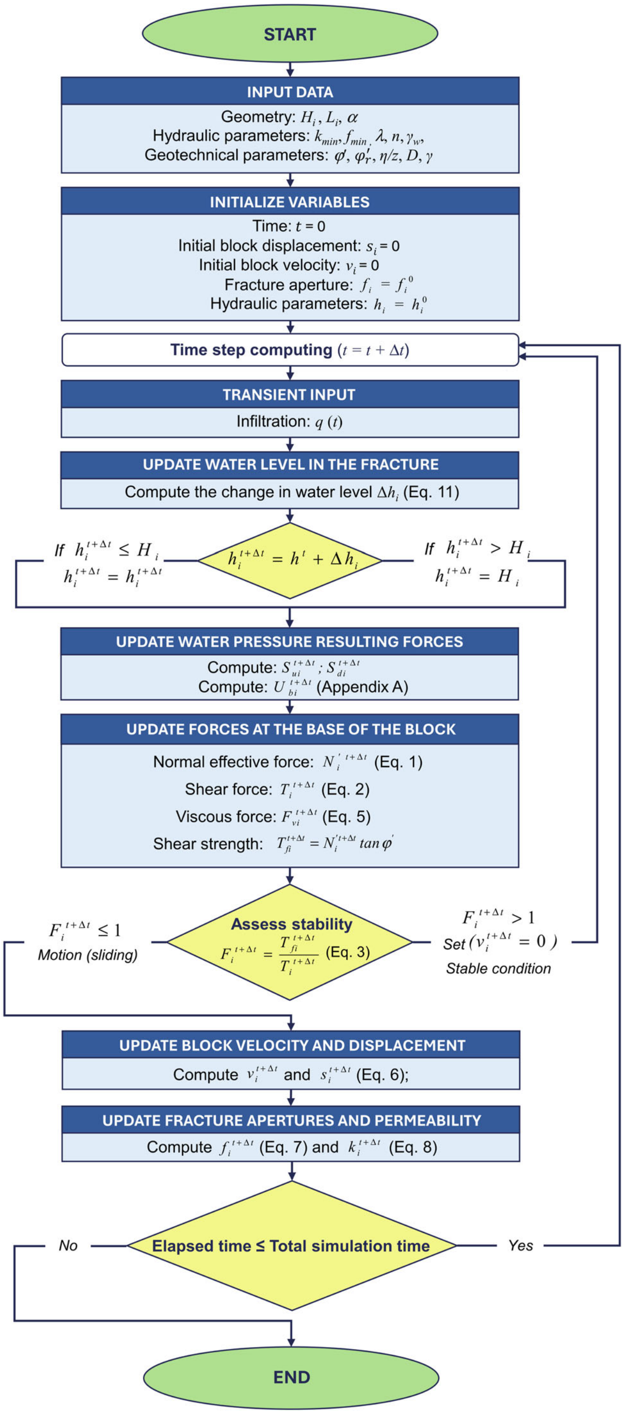

Fig. 16 Workflow of the Finite-Difference-Based algorithm implemented for a single block

pressure distribution at the base of block at $t = \infty$) is the same in all three considered scenarios.

Appendix B Finite difference-based algorithm workflow

The workflow of the finite difference base algorithm implemented for a single block is reported in Fig. 16.

Author contributions Alessio Ferrari: formal analysis, conceptualisation; methodology; Writing – original draft; software; Writing – review & editing; funding acquisition; Supervision. Marco Rosone: formal analysis, conceptualisation; methodology; Writing – original draft; investigation; software; Writing – review & editing. Giorgio Manno: Writing – original draft; Writing – review & editing; investigation; data curation; geological and geomorphological supervision. Maurizio Ziccarelli: Writing – review & editing; supervision. Alessandro Corsini: conceptualisation; Writing – review & editing; geological and geomorphological supervision. Francesco Ronchetti: conceptualisation; Writing – review & editing; geological and geomorphological supervision.

Funding Open access funding provided by Università degli Studi di Palermo within the CRUI-CARE Agreement. This study was carried out within the RETURN Extended Partnership and received funding from the European Union Next–GenerationEU (National Recovery and Resilience Plan – NRRP, Mission 4, Component 2, Investment 1.3 – D.D. 1243 2/8/2022, PE0000005).

Data availability The software developed in this work is available from the authors upon request.

Declarations

Conflict of interest The authors have no competing interests to declare that are relevant to the content of this article.

References

1. Angeli MG, Gasparetto P, Menotti RM, Pasuto A, Silvano S (1997) A visco–plastic model for slope analysis applied to a mudslide in Cortina d'Ampezzo, Italy. Q J Eng Geol 29:233–240. https://doi.org/10.1144/GSL.QJEGH.1996.029.P3.06
2. Alonso EE, Gens A (2006) Aznalcóllar dam failure. Part 3: Dynamics of the motion. Geotechnique 56:203–210. https://doi.org/10.1680/geot.2006.56.3.203
3. Babuska I, Oden JT (2004) Verification and validation in computational engineering and science: basic concepts. Comput Methods Appl Mech Eng 193(36–38):4057–4066. https://doi.org/10.1016/j.cma.2004.03.002
4. Carlà T, Gigli G, Lombardi L et al (2024) Mechanisms of block instability at the toe of a slowly deforming rock slope. Rock Mech Rock Eng 57:1543–1563. https://doi.org/10.1007/s00603-023-03674-9
5. Corominas J, Moya J, Ledesma A, Lloret A, Gili JA (2005) Prediction of ground displacements and velocities from groundwater level changes at the Vallcebre landslide (Eastern Pyrenees, Spain). Landslides 2:83–96. https://doi.org/10.1007/s10346-005-0049-1
6. Corsini A, Castagnetti C, Bertacchini E, Rivola R, Ronchetti F, Capra A (2013) Integrating airborne and multi-temporal long-range terrestrial laser scanning with total station measurements for mapping and monitoring a compound slow moving rockslide. Earth Surf Process Landf 38:1330–1338. https://doi.org/10.1002/esp.3445
7. Corsini A, Bonacini F, Mulas M, Petitta M, Ronchetti F, Truffelli G (2015) Long–term continuous monitoring of a deep–seated compound rockslide in the Northern Apennines (Italy). In Engineering geology for society and territory, vol 2, pp 1337–1340. https://doi.org/10.1007/978-3-319-09057-3_235
8. Corsini A, Mulas M (2017) Use of ROC curves for early warning of landslide displacement rates in response to precipitation (Piagneto landslide, Northern Apennines, Italy). Landslides 14:1241–1252. https://doi.org/10.1007/s10346-016-0781-8
9. Deng Y, Fan X, Scaringi G, Wang D, He S (2024) Assessing the efficiency of thermochemical pressurization in the Jiweishan rockslide. Rock Mech Rock Eng 57:793–806. https://doi.org/10.1007/s00603-023-03639-y
10. de Moura CA, Carlos S, Kubrusly CS (2013) The Courant–Friedrichs–Lewy (CFL) condition. Birkhäuser Boston, MA. https://doi.org/10.1007/978-0-8176-8394-8
11. Ferrari A, Ledesma A, González DA, Corominas J (2011) Effects of the foot evolution on the behaviour of slow–moving landslides. Eng Geol 117:217–228. https://doi.org/10.1016/j.enggeo.2010.11.001
12. Hoek E, Bray JW (1981) Rock slope engineering, Revised 3rd Edition. The Institution of Mining and Metallurgy, London, pp 341–351
13. Hungr O, Leroueil S, Picarelli L (2014) The Varnes classification of landslide types, an update. Landslides 11:167–194. https://doi.org/10.1007/s10346-013-0436-y
14. Krzeminska DM, Bogaard TA, Van Asch TW, Van Beek LPH (2012) A conceptual model of the hydrological influence of fissures on landslide activity. Hydrol Earth Syst Sci 16:1561–1576. https://doi.org/10.5194/hess-16-1561-2012
15. Laloui L, Ferrari A, Li C, Eichenberger J (2016) Hydro–mechanical analysis of volcanic ash slopes during rainfall. Géotechnique 66(3):220–231. https://doi.org/10.1680/jgeot.15.LM.001
16. Lambe TW, Withman RV (1969) Soil mechanics. John Wiley & Sons, New York
17. Ledesma A, Corominas J, Gonzàles A, Ferrari A (2009) Modelling slow moving landslides controlled by rainfall. In: Proceedings of the 1st Italian Work Landslides, Napoli, Italy, 8–10 June, vol 1, pp 196–205
18. Lewy H, Friedrichs K, Courant R (1928) Über die partiellen Differenzengleichungen der mathematischen Physik. Math Ann 100(1928):32–74

19. Oberkampf WL, Trucano TG, Hirsch C (2004) Verification, validation, and predictive capability in computational engineering and physics. Appl Mech Rev 57(5):345–384. https://doi.org/10.1115/1.1767847
20. Picarelli L, Urciuoli G, Russo C (2004) Effect of groundwater regime on the behaviour of clayey slopes. Can Geotech J 41:467–484. https://doi.org/10.1139/t04-009
21. Rollo F, Buscarnera G (2023) Modelling seasonal landslide motion: does it only depend on fluctuations in normal effective stress? Int J Numer Anal Methods Geomech 47:3331–3350. https://doi.org/10.1002/nag.3625
22. Rosone M, Ziccarelli M, Ferrari A (2020) Displacement evolution of a large landslide in a highly fissured clay. Lect Notes Civ Eng 40:195–204. https://doi.org/10.1007/978-3-030-21359-6_21
23. Schwer LE (2007) An overview of the PTC 60/V&V 10: guide for verification and validation in computational solid mechanics: Transmitted by Le Schwer, chair PTC 60/V&V 10. Eng Comput 23(4):245–252. https://doi.org/10.1007/s00366-007-0072-z
24. Soga K, Alonso E, Yerro A, Kumar K, Bandara S (2016) Trends in large–deformation analysis of landslide mass movements with particular emphasis on the material point method. Géotechnique 66(3):248–273. https://doi.org/10.1680/jgeot.15.LM.005
25. Song J, Lu Z, Pan Y, Ji J, Gao Y (2024) Investigation of seismic displacements in bedding rock slopes by an extended Newmark sliding block model. Landslides 21(3):461–477. https://doi.org/10.1007/s10346-023-02170-z
26. Spreafico MC, Francioni M, Cervi F et al (2015) Back analysis of the 2014 San Leo landslide using combined terrestrial laser scanning and 3D distinct element modelling. Rock Mech Rock Eng 49:2235–2251. https://doi.org/10.1007/s00603-015-0763-5
27. Skempton AW, Hutchinson JN (1969) Stability of natural slopes. In: Proceedings of the 7th international conference on soil mechanics and foundation engineering, Mexico City, State of the Art, 291–340
28. Sun W (2019) Verification & validation of computational models associated with the mechanics of materials. Metals & Materials Society. https://doi.org/10.7449/VandV_1
29. Tacher L, Bonnard CH, Laloui L, Le Parriaux A (2005) Modelling the behaviour of a large landslide with respect to hydrogeological and geomechanical parameter heterogeneity. Landslides 2:3–14
30. Tacher L, Bonnard C, Laloui L, Parriaux A (2005) Modelling the behaviour of a large landslide with respect to hydrogeological and geomechanical parameter heterogeneity. Landslides 2(1):3–14. https://doi.org/10.1007/s10346-004-0038-9
31. Troncone A, Pugliese L, Lamanna G, Conte E (2021) Prediction of rainfall–induced landslide movements in the presence of stabilizing piles. Eng Geol 288:106143. https://doi.org/10.1016/j.enggeo.2021.106143
32. Van Asch TWJ, Van Beek LPH, Bogaard TA (2007) Problems in predicting the mobility of slow–moving landslides. Eng Geol 91(1):46–55. https://doi.org/10.1016/j.enggeo.2006.12.012
33. Van Beek LPH, Van Asch TWJ (1999) A combined conceptual model for the effects of fissure–induced infiltration on slope stability. In: Hergarten S, Neugebauer HJ (ed) Process modelling and landform evolution. Lecture Notes in Earth Sciences, Springer, Berlin, Heidelberg, vol 78, pp 147–167. https://doi.org/10.1007/BFb0009724
34. Zhou Y, Zhao X (2024) Progressive failure mechanism and stability for a rockslide with a toe rock bridge. Landslides 21(7):1691–1706. https://doi.org/10.1007/s10346-024-02251-7